CMS-BPH-21-001

arXiv:2212.02309v1 [hep-ex] 5 Dec 2022

Measurement of the dependence of the hadron production fraction ratio f_s/f_u on B meson kinematic variables in proton-proton collisions at $\sqrt{s} = 13$ TeV

The CMS Collaboration

Abstract

The dependence of the ratio between the B_s^0 and B^+ hadron production fractions, f_s/f_u, on the transverse momentum (p_T) and rapidity of the B mesons is studied using the decay channels $B_s^0 \to J/\psi\,\phi$ and $B^+ \to J/\psi\,K^+$. The analysis uses a data sample of proton-proton collisions at a center-of-mass energy of 13 TeV, collected by the CMS experiment in 2018 and corresponding to an integrated luminosity of 61.6 fb^{-1}. The f_s/f_u ratio is observed to depend on the B p_T and to be consistent with becoming asymptotically constant at large p_T. No rapidity dependence is observed. The ratio of the B^0 to B^+ hadron production fractions, f_d/f_u, measured using the $B^0 \to J/\psi\,K^{*0}$ decay channel, is found to be consistent with unity and independent of p_T and rapidity.

Submitted to Physical Review Letters

Precise knowledge of the hadron production fractions is essential for measuring b hadron decay rates at the LHC. In particular, one of the main systematic uncertainties affecting the measurement of the branching fraction of the rare $B_s^0 \rightarrow \mu^+\mu^-$ decay is the uncertainty in the relative production yields of the B_s^0 and B^+ mesons, which is directly related to the ratio of the respective hadron fractions, f_s/f_u [1–5]. The relative abundances of b hadrons (B^+, B^0, B_s^0, and Λ_b^0) have been measured at LEP in electron-positron collisions [6–9] and at the Tevatron in proton-antiproton collisions [10], the two sets of results being consistent with each other [11] and with theoretical expectations [12]. More recently, the LHCb Collaboration, using large event samples of proton-proton (pp) collisions at $\sqrt{s} = 7$, 8, and 13 TeV, was able to study how the b hadron abundances depend on their transverse momentum (p_T). In particular, the b baryon fraction (f_{baryon}, derived from the Λ_b^0 yields) decreases by around a factor of 2, with respect to the B^+ and B^0 fractions, from 5 to 25 GeV, a clear observation of a p_T-dependence of a b hadron fraction [13]. Considering that $f_u + f_d + f_s + f_{baryon} = 1$, neglecting the very small contributions of b hadrons made of several heavy quarks, it is reasonable to expect that also the B meson fractions are p_T-dependent. Indeed, LHCb has also reported a significant p_T dependence of the ratio between the B_s^0 and B^+ fragmentation fractions [14], in the 2.0–4.5 rapidity (y) range and at relatively low p_T. On the other hand, the ATLAS Collaboration reported a measurement consistent with no p_T dependence, albeit for a different region of p_T and y [15].

This Letter presents an analysis aimed at establishing if and how the relative B_s^0 and B^+ production rates change with p_T in a kinematic region relevant for the ATLAS and CMS experiments at the CERN LHC, $p_T > 12$ GeV and $|y| < 2.4$, approximately complementary to that of the LHCb detector. The measurement uses a sample of pp collisions collected by the CMS experiment in 2018 at a center-of-mass energy of 13 TeV and corresponding to an integrated luminosity of 61.6 fb^{-1} [16, 17].

Throughout this Letter, charge-conjugate states are implicitly included, and K^{*0} and ϕ represent the $K^{*0}(892)$ and $\phi(1020)$, respectively. The B^+ and B_s^0 mesons are reconstructed using the $B^+ \rightarrow J/\psi\, K^+$ and $B_s^0 \rightarrow J/\psi\, \phi$ decay channels, with the J/ψ and ϕ mesons decaying as $J/\psi \rightarrow \mu^+\mu^-$ and $\phi \rightarrow K^+K^-$. The respective event yields, N_{B+} and $N_{B_s^0}$, are measured with corresponding detection efficiencies ϵ_{B+} and $\epsilon_{B_s^0}$. The ratio of the efficiency-corrected meson yields, $\mathcal{R}_s = (N_{B_s^0}/\epsilon_{B_s^0}) / (N_{B+}/\epsilon_{B+})$, is directly proportional to the f_s/f_u ratio,

$$\mathcal{R}_s = f_s/f_u \, \frac{\mathcal{B}(B_s^0 \rightarrow J/\psi\, \phi)\mathcal{B}(\phi \rightarrow K^+K^-)}{\mathcal{B}(B^+ \rightarrow J/\psi\, K^+)}, \tag{1}$$

where $\mathcal{B}(B_s^0 \rightarrow J/\psi\, \phi)$, $\mathcal{B}(\phi \rightarrow K^+K^-)$, and $\mathcal{B}(B^+ \rightarrow J/\psi\, K^+)$ are the branching fractions of the indicated decay channels; the $\mathcal{B}(J/\psi \rightarrow \mu^+\mu^-)$ factor cancels in the ratio. Given that the available measurements of the $B_s^0 \rightarrow J/\psi\, \phi$ branching fraction and of f_s are correlated, we report measurements of $\mathcal{R}_s$ rather than of f_s/f_u.

The analysis also includes a measurement of the ratio between the B^0 and B^+ hadron fractions, f_d/f_u, using the B^0 yield determined with $B^0 \rightarrow J/\psi\, K^{*0}$ events, where the K^{*0} mesons are reconstructed in the $K^{*0} \rightarrow \pi^-K^+$ decay channel. Using notations analogous to those used above,

$$\mathcal{R}_d = \frac{N_{B0}}{\epsilon_{B0}} \bigg/ \frac{N_{B+}}{\epsilon_{B+}} = f_d/f_u \, \frac{\mathcal{B}(B^0 \rightarrow J/\psi\, K^{*0})\mathcal{B}(K^{*0} \rightarrow \pi^-K^+)}{\mathcal{B}(B^+ \rightarrow J/\psi\, K^+)}. \tag{2}$$

Under the assumption of strong isospin symmetry, the f_d/f_u ratio is predicted to be independent of kinematic variables [18], and identical to unity. Given that the branching fractions used

to calculate $f_\mathrm{d}/f_\mathrm{u}$ from $\mathcal{R}_\mathrm{d}$ are (independently) obtained from high precision B factory measurements (under the assumption of isospin invariance), we report the more relevant quantity $f_\mathrm{d}/f_\mathrm{u}$.

The CMS apparatus is a multipurpose detector [19] designed to trigger on and identify electrons, muons, photons, and (charged and neutral) hadrons [20–22]. A superconducting solenoid of 6 m internal diameter provides a magnetic field of 3.8 T. Within the solenoid volume are the silicon pixel and strip tracker, a crystal electromagnetic calorimeter, and a brass and scintillator hadron calorimeter. Muons are measured in gas-ionization detectors embedded in the steel flux-return yoke outside the solenoid. Events of interest are selected using a two-tiered trigger system. The first level, composed of custom hardware processors, uses information from the calorimeters and muon detectors to select events at a rate of 100 kHz within a fixed latency of about 4 μs [23]. The second level, consisting of a farm of processors running a faster version of the full event reconstruction software, reduces the rate to around 1 kHz, before data storage [24].

The events used in the analysis were selected by a trigger requiring two oppositely charged muons with pseudorapidity $|\eta| < 2.5$ and $p_\mathrm{T} > 4$ GeV, a distance of closest approach between the two muons smaller than 0.5 cm, a dimuon vertex fit χ^2 probability larger than 10%, a dimuon invariant mass in the range 2.9–3.3 GeV, and a transverse distance between the dimuon vertex and the beam axis, L_{xy}, larger than three times its uncertainty. In addition, the dimuon $\vec{p}_\mathrm{T}$ and transverse displacement vector, $\vec{L}_{xy}$, must be aligned with each other: $\cos\theta \equiv \vec{L}_{xy} \cdot \vec{p}_\mathrm{T}/(L_{xy}\, p_\mathrm{T}) > 0.9$. The trigger also requires a third track in the event, compatible with being produced at the dimuon vertex, having $p_\mathrm{T} > 1.2$ GeV and a transverse impact parameter significance larger than 2. Finally, the dimuon-plus-track vertex fit χ^2 probability must be larger than 10%.

The charged tracks used to reconstruct the B mesons must pass high-purity criteria [22], have five or more hits in the silicon tracker, at least one of them in the pixel layers, and have $|\eta| < 2.4$. They must also match the tracks that triggered the data readout. The muons used to reconstruct the J/ψ candidates must fulfill soft-muon identification requirements [21], which include the (loose) matching between the track reconstructed in the silicon tracker and the one reconstructed in the muon detectors. They must also have $p_\mathrm{T} > 4$ GeV and an impact parameter smaller than 0.3 cm in the transverse plane and smaller than 20 cm along the beam axis.

The J/ψ candidate is combined with one track to reconstruct $\mathrm{B}^+ \to \mathrm{J}/\psi\,\mathrm{K}^+$ decays or with a pair of oppositely charged tracks to reconstruct the $\mathrm{B}^0_\mathrm{s} \to \mathrm{J}/\psi\,\phi$ and $\mathrm{B}^0 \to \mathrm{J}/\psi\,\mathrm{K}^{*0}$ decays. All three tracks must have $p_\mathrm{T} > 1.2$ GeV. They are fitted together with the dimuon, imposing a common (secondary) vertex (SV, the B meson decay point), constraining the dimuon invariant mass to the J/ψ world-average mass, $m^\mathrm{PDG}_{\mathrm{J}/\psi}$ [25], and assigning to each of the other tracks the $\pi^\pm$ or $\mathrm{K}^\pm$ masses, as suitable. Furthermore, the invariant mass of the pair of tracks must satisfy $|M(\mathrm{K}^+\mathrm{K}^-) - m^\mathrm{PDG}_\phi| < 10$ MeV for B^0_s decays and $|M(\pi\mathrm{K}) - m^\mathrm{PDG}_{\mathrm{K}^{*0}}| < 50$ MeV for B^0 decays, where m^PDG_ϕ and $m^\mathrm{PDG}_{\mathrm{K}^{*0}}$ are, respectively, the ϕ and K^{*0} world-average masses [25]. In the latter case, two combinations are possible ($\pi^+\mathrm{K}^-$ and $\mathrm{K}^+\pi^-$); if both match the mass window requirement, only the one with mass closer to $m^\mathrm{PDG}_{\mathrm{K}^{*0}}$ is kept.

The primary vertex (PV) is selected among the several reconstructed pp collisions as the one that minimizes the pointing angle of the B meson, defined as the angle between the B momentum and the vector joining the primary and secondary vertices. The PV is refitted without the tracks of the B candidate before computing the B decay length as the distance between the PV

and the SV. We select B meson candidates with $12 < p_T < 70$ GeV, $|y| < 2.4$, a decay length larger than five times its uncertainty, and a dimuon-plus-track(s) vertex χ^2 probability larger than 10%. For each decay channel, if more than one B meson candidate is reconstructed in an event (occurring in less than 1% of the events), only the one with the highest fit χ^2 probability is kept.

The event selection criteria described above were optimized through the study of Monte Carlo (MC) event samples, which were also used to evaluate the detection efficiencies and the shapes of the invariant mass distributions of some background contributions. They were generated with PYTHIA 8.230 [26] for the production and hadronization steps, with EVTGEN 1.6.0 [27] for the decay of the b hadrons, and with PHOTOS 3.61 [28] for the final-state radiation modeling. The response of the CMS detector to the generated events, including the trigger and reconstruction steps, was simulated with GEANT4 [29], using algorithms identical to those used on the data. The simulated events include multiple pp interactions in the same or nearby beam crossings, with a distribution matching the one observed in the collected data.

The B_s^0, B^+, and B^0 meson yields are measured by fitting, with unbinned maximum likelihood techniques, the $J/\psi\,\phi$, $J/\psi\,K^+$, and $J/\psi\,K^{*0}$ invariant mass distributions, respectively. These distributions are fitted for 12 p_T bins (integrated over y) or 7 $|y|$ bins (integrated over p_T), with ranges defined so as to keep a similar number of events in each bin. Figure 1 shows the three invariant mass distributions for the 20–23 GeV p_T bin.
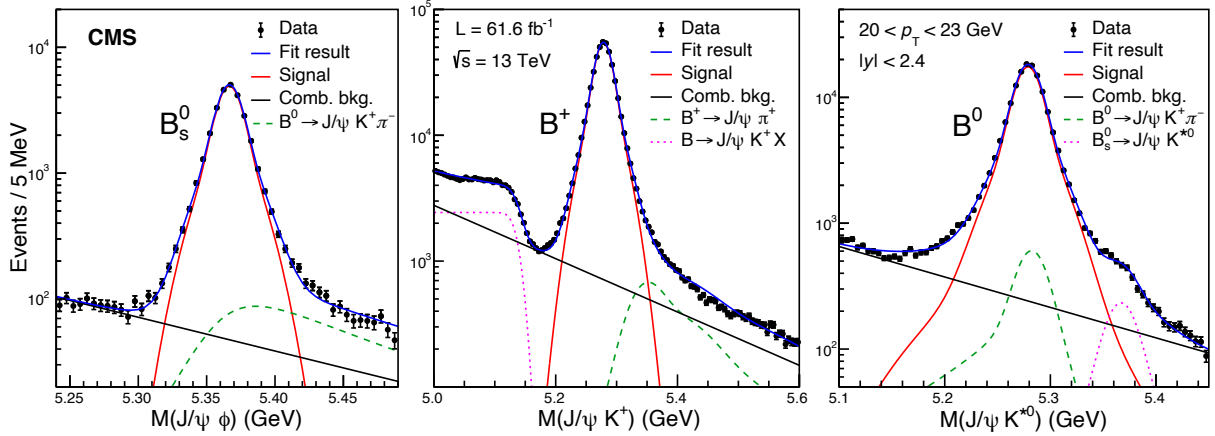

Figure 1: The $J/\psi\,\phi$, $J/\psi\,K^+$, and $J/\psi\,K^{*0}$ invariant mass distributions for B meson candidates with $20 < p_T < 23$ GeV, and associated fits as described in the text.

The signal peak is fitted by the sum of two Gaussian functions with a common mean and independent widths. The underlying combinatorial background is fitted by an exponential function. The $J/\psi\,K^+$ sample includes a background term due to events where B mesons decay through $J/\psi\,K^+\,X$ channels and the X particle is not reconstructed. This contribution is described by an error function, with two free shape parameters. Some of the $J/\psi\,K^{*0}$ candidates have swapped pion-kaon mass assignments. They are included in the fit model by adding a component with shape and normalization (12% relative to the unswapped yield) fixed from simulation. The $J/\psi\,K^{*0}$ sample also includes (Cabibbo-suppressed) $B_s^0 \to J/\psi\,K^{*0}$ decays, with normalization as a free parameter and described by a shape identical to that of the B^0 signal peak, except for the shifted mass and for a small width broadening to account for the change of mass resolution, as determined from simulation.

All the other background contributions have shapes determined from the simulated event samples. The $B^+ \to J/\psi\,\pi^+$ curve in the B^+ panel represents (Cabibbo-suppressed) decays where

the pion track is misinterpreted as a kaon; its normalization is fixed to that of the B^+ signal yield, scaled by the ratio of the two branching fractions [25]. The misidentification of a pion as a kaon is also the reason why sometimes a $B^0 \to J/\psi\, K\, \pi$ decay is incorrectly assigned to the B_s^0 sample. This small contribution is described by a Johnson function [30], with a normalization fixed, in each p_T or $|y|$ bin, to that of the B_s^0 signal yield, the scaling factor being the relative yield found in a fit to the integrated event sample. The background to the B_s^0 sample from $\Lambda_b^0 \to J/\psi\, K^-\, p$ decays where the proton is misidentified as a kaon has been found to be negligible. A background from $B^0 \to J/\psi\, K\, \pi$ decays also contributes to the $B^0 \to J/\psi\, K^{*0}$ distributions. This peaking background is modeled with a double-sided Crystal Ball [31] function plus a Gaussian function. Its normalization is fixed, in each p_T or $|y|$ bin, to that of the B^0 signal yield, scaled by the yield ratio obtained in the fit of the integrated event sample.

As seen in Eqs. (1) and (2), only the *ratios* of detection efficiencies, $\epsilon_{B_s^0} / \epsilon_{B+}$ and $\epsilon_{B0} / \epsilon_{B+}$, are needed to convert the ratios of signal event yields, obtained from the fits illustrated in Fig. 1, into the $\mathcal{R}_s$ and $\mathcal{R}_d$ observables. These efficiency ratios are evaluated using the simulated event samples, reflecting the trigger and reconstruction steps, as well as the detector acceptance. Both ratios increase by around a factor of 3.5 between the lowest and highest p_T bins, while the variation with $|y|$ is only at the 10% level.

The $\mathcal{R}_s$ and $\mathcal{R}_d$ measurements are affected by systematic uncertainties in the determination of the fitted signal yields and in the evaluation of the efficiency ratios.

The systematic uncertainties affecting the signal yields are evaluated by repeating the fits of the mass distributions in alternative conditions and computing the difference between the obtained results and those of the baseline fit. Two main variations of the fit model are independently considered: first, the modeling of the signal peaks is changed from the default double-Gaussian to a Student's t-distribution [32]; second, the combinatorial background is fitted by a first-order Chebyshev polynomial instead of the baseline exponential function. An additional systematic uncertainty in the B^0 meson yield, of less than 1%, is evaluated by fitting the $J/\psi\, K^{*0}$ mass distribution changing the normalization of the "π–K swap" term, relative to that of the B^0 signal term, by the uncertainty in the default value, which exclusively reflects the sizes of the MC event samples; other systematic effects were found to be negligible. The fit procedure itself is seen to provide unbiased results, for each of the bins, both for the central values and the uncertainties, through a study involving fits of 1000 event samples randomly generated using the nominal functions with the best fit parameters and with sizes corresponding to the number of measured events. The result is that the uncertainties in the fitted B_s^0, B^+, and B^0 signal yields contribute systematic uncertainties to the $\mathcal{R}_s$ and $\mathcal{R}_d$ measurements that are, respectively, in the 1.6–2.6% and 2.0–5.0% ranges.

For the efficiency ratios, $\epsilon_{B_s^0} / \epsilon_{B+}$ and $\epsilon_{B0} / \epsilon_{B+}$, a systematic uncertainty, $\approx$1% for all p_T and $|y|$ bins, reflects the size of the simulated event samples. Given that the B_s^0 and B^0 decays lead to one more track than the B^+ decays, a 2.3% uncertainty is assigned to both efficiency ratios, corresponding to the uncertainty in the single-track reconstruction efficiency [33]; this uncertainty is assumed to be common to all the p_T and $|y|$ bins. Several other potential sources of uncertainty were considered and found to have negligible effects on the efficiency *ratios*. The muon identification and reconstruction efficiencies, in particular, cancel out. The efficiencies were also recomputed with varied B_s^0 p_T distributions and with the decay angular distributions reweighed to match the data; both variations have negligible effects. Finally, the simulated events were reweighed (with weights dependent on the y and p_T of the B meson, as well as on the p_T of the kaons) so that the B_s^0, B^+, and B^0 MC distributions match the measured ones. This procedure leads to systematic uncertainties in the 1–2% and 2–5% ranges for the $\mathcal{R}_s$ and $\mathcal{R}_d$

measurements, respectively.

Apart from the uncertainty in the track reconstruction efficiency, assumed to be independent of p_T and $|y|$, the bin-to-bin systematic uncertainties are added in quadrature. For the $\mathcal{R}_s$ measurement, they are in the 2.3–3.2% and 1.8–4.4% ranges for the p_T and $|y|$ results, respectively, while for $\mathcal{R}_d$ the corresponding ranges are 2.4–7.8% and 2.3–4.9%. The larger $\mathcal{R}_d$ uncertainties arise from the more complex background composition of the B^0 decay. Both measurements have $\approx 1\%$ statistical uncertainties in each bin.
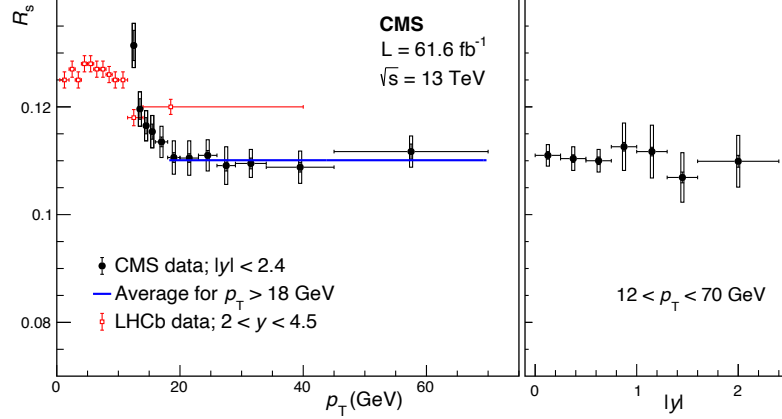

Figure 2: Efficiency-corrected yield ratio $\mathcal{R}_s$, as a function of p_T (left) and $|y|$ (right). The vertical bars (boxes) represent the statistical (bin-to-bin systematic) uncertainties, while the horizontal bars give the bin widths. The global uncertainty (of 2.3%) is not graphically represented. The blue line represents the average for $p_T > 18$ GeV. For comparison, the LHCb measurement [14] is also shown.

The measured $\mathcal{R}_s$ values, presented in Fig. 2, do not show any signs of a rapidity dependence. In contrast, they show a clear p_T-dependence at low p_T, followed by a flat high-p_T trend. Averaging the $p_T > 18$ GeV measurements gives $\mathcal{R}_s = 0.1102 \pm 0.0027$, where the uncertainty includes all contributions, added in quadrature. The LHCb measurements of $\mathcal{R}_s$ versus p_T (for $2 < y < 4.5$), also shown in Fig. 2, are compatible with the CMS data and reinforce the observed p_T dependence.

Figure 3 displays the measured f_d/f_u ratio as a function of p_T and $|y|$, using Eq. (2) to convert from $\mathcal{R}_d$. No dependence on p_T or $|y|$ is observed. The average over all the p_T points is 1.015 ± 0.051, where the uncertainty reflects all contributions, added in quadrature, including the branching fraction uncertainties [25]. This value is consistent with unity, as expected from strong isospin symmetry.

The numerical results corresponding to Figs. 2 and 3 are tabulated in Appendix A and in the HEPData record for this analysis [34].

In summary, the ratio of the B_s^0 and B^+ hadron production fractions, f_s/f_u, directly proportional to the ratio of the efficiency-corrected meson yields, $\mathcal{R}_s$, is studied as a function of the B meson transverse momentum p_T and rapidity, using the $B_s^0 \to J/\psi\,\phi$ and $B^+ \to J/\psi\,K^+$ decay channels. The analysis uses an event sample of pp collisions at a center-of-mass energy of 13 TeV, collected by CMS in 2018 and corresponding to an integrated luminosity of 61.6 fb^{-1}. While no $\mathcal{R}_s$ dependence on the B meson rapidity is seen, a strong variation is observed in the $12 < p_T < 18$ GeV range, followed by a flat trend for higher p_T values. The f_d/f_u ratio, measured using the $B^0 \to J/\psi\,K^{*0}$ decay channel, is found to be compatible with unity and independent of rapidity and p_T, as predicted by strong isospin symmetry. The b hadron pro-
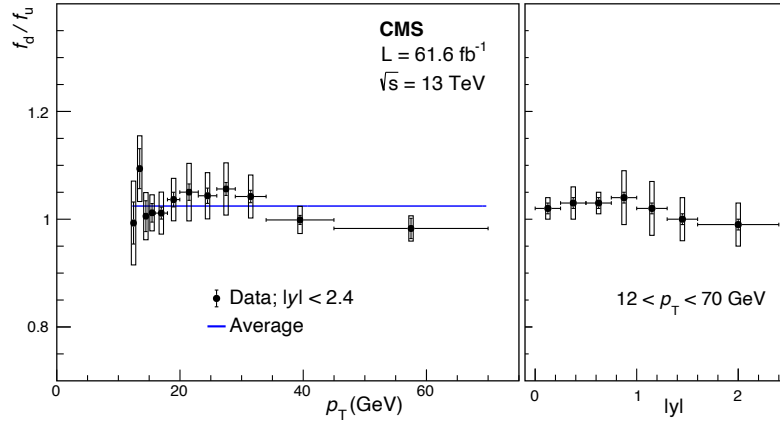
Figure 3: The ratio of the B^0 to B^+ hadron production fractions f_d/f_u, as a function of p_T (left) and $|y|$ (right). The vertical bars (boxes) represent the statistical (bin-to-bin systematic) uncertainties, while the horizontal bars give the bin widths. The global uncertainty (of 4.9%) is not graphically represented. The blue line represents the average of all the points.

duction fractions presented in this Letter provide a crucial input to measurements by ATLAS and CMS of the $B_s^0 \to \mu^+\mu^-$ branching fraction.

References

[1] CMS and LHCb Collaborations, "Observation of the rare $B_s^0 \to \mu^+\mu^-$ decay from the combined analysis of CMS and LHCb data", *Nature* **522** (2015) 68, doi:10.1038/nature14474, arXiv:1411.4413.

[2] ATLAS Collaboration, "Study of the rare decays of B_s^0 and B^0 mesons into muon pairs using data collected during 2015 and 2016 with the ATLAS detector", *JHEP* **04** (2019) 098, doi:10.1007/JHEP04(2019)098, arXiv:1812.03017.

[3] CMS Collaboration, "Measurement of properties of $B_s^0 \to \mu^+\mu^-$ decays and search for $B^0 \to \mu^+\mu^-$ with the CMS experiment", *JHEP* **04** (2020) 188, doi:10.1007/JHEP04(2020)188, arXiv:1910.12127.

[4] LHCb Collaboration, "Measurement of the $B_s^0 \to \mu^+\mu^-$ branching fraction and effective lifetime and search for $B^0 \to \mu^+\mu^-$ decays", *Phys. Rev. Lett.* **118** (2017) 191801, doi:10.1103/PhysRevLett.118.191801, arXiv:1703.05747.

[5] LHCb Collaboration, "Measurement of the $B_s^0 \to \mu^+\mu^-$ decay properties and search for the $B^0 \to \mu^+\mu^-$ and $B_s^0 \to \mu^+\mu^-\gamma$ decays", *Phys. Rev. D* **105** (2022) 012010, doi:10.1103/PhysRevD.105.012010, arXiv:2108.09283.

[6] OPAL Collaboration, "Evidence for the existence of the strange b-flavoured meson B_s^0 in Z^0 decays", *Phys. Lett. B* **295** (1992) 357, doi:10.1016/0370-2693(92)91578-W.

[7] ALEPH Collaboration, "Measurement of the B_s^0 lifetime and production rate with $D_s^-\ell^+$ combinations in Z decays", *Phys. Lett. B* **361** (1995) 221, doi:10.1016/0370-2693(95)01173-N.

[8] L3 Collaboration, "Measurements of the $b\bar{b}$ production cross-section and forward backward asymmetry at center-of-mass energies above the Z pole at LEP", *Phys. Lett. B* **485** (2000) 71, doi:10.1016/S0370-2693(00)00676-6, arXiv:hep-ex/0005023.

[9] DELPHI Collaboration, "A measurement of the branching fractions of the b-quark into charged and neutral b-hadrons", *Phys. Lett. B* **576** (2003) 29, `doi:10.1016/j.physletb.2003.09.070`, `arXiv:hep-ex/0311005`.

[10] CDF Collaboration, "Measurement of ratios of fragmentation fractions for bottom hadrons in $p\bar{p}$ collisions at $\sqrt{s} = 1.96\,\text{TeV}$", *Phys. Rev. D* **77** (2008) 072003, `doi:10.1103/PhysRevD.77.072003`, `arXiv:0801.4375`.

[11] HFLAV Collaboration, "Averages of b-hadron, c-hadron, and τ-lepton properties as of 2018", *Eur. Phys. J. C* **81** (2021) 226, `doi:10.1140/epjc/s10052-020-8156-7`, `arXiv:1909.12524`.

[12] B. Mele and P. Nason, "The fragmentation function for heavy quarks in QCD", *Nucl. Phys. B* **361** (1991) 626, `doi:10.1016/0550-3213(91)90597-Q`. [Erratum: `doi:10.1016/0550-3213(91)90597-Q`].

[13] LHCb Collaboration, "Measurement of b-hadron fractions in 13 TeV pp collisions", *Phys. Rev. D* **100** (2019) 031102, `doi:10.1103/PhysRevD.100.031102`, `arXiv:1902.06794`.

[14] LHCb Collaboration, "Measurement of f_s/f_u variation with proton-proton collision energy and B-meson kinematics", *Phys. Rev. Lett.* **124** (2020) 122002, `doi:10.1103/PhysRevLett.124.122002`, `arXiv:1910.09934`.

[15] ATLAS Collaboration, "Determination of the ratio of b-quark fragmentation fractions f_s/f_d in pp collisions at $\sqrt{s} = 7\,\text{TeV}$ with the ATLAS detector", *Phys. Rev. Lett.* **115** (2015) 262001, `doi:10.1103/PhysRevLett.115.262001`, `arXiv:1507.08925`.

[16] CMS Collaboration, "CMS luminosity measurement for the 2018 data-taking period at $\sqrt{s} = 13\,\text{TeV}$", CMS Physics Analysis Summary CMS-PAS-LUM-18-002, 2019.

[17] CMS Collaboration, "Precision luminosity measurement in proton-proton collisions at $\sqrt{s} = 13\,\text{TeV}$ in 2015 and 2016 at CMS", *Eur. Phys. J. C* **81** (2021) 800, `doi:10.1140/epjc/s10052-021-09538-2`, `arXiv:2104.01927`.

[18] M. Jung, "Branching ratio measurements and isospin violation in B-meson decays", *Phys. Lett. B* **753** (2016) 187, `doi:10.1016/j.physletb.2015.12.024`, `arXiv:1510.03423`.

[19] CMS Collaboration, "The CMS experiment at the CERN LHC", *JINST* **3** (2008) S08004, `doi:10.1088/1748-0221/3/08/S08004`.

[20] CMS Collaboration, "Electron and photon reconstruction and identification with the CMS experiment at the CERN LHC", *JINST* **16** (2021) P05014, `doi:10.1088/1748-0221/16/05/P05014`, `arXiv:2012.06888`.

[21] CMS Collaboration, "Performance of the CMS muon detector and muon reconstruction with proton-proton collisions at $\sqrt{s} = 13\,\text{TeV}$", *JINST* **13** (2018) P06015, `doi:10.1088/1748-0221/13/06/P06015`, `arXiv:1804.04528`.

[22] CMS Collaboration, "Description and performance of track and primary-vertex reconstruction with the CMS tracker", *JINST* **9** (2014) P10009, `doi:10.1088/1748-0221/9/10/P10009`, `arXiv:1405.6569`.

[23] CMS Collaboration, "Performance of the CMS Level-1 trigger in proton-proton collisions at $\sqrt{s} = 13\,\text{TeV}$", *JINST* **15** (2020) P10017, `doi:10.1088/1748-0221/15/10/P10017`, `arXiv:2006.10165`.

[24] CMS Collaboration, "The CMS trigger system", *JINST* **12** (2017) P01020, `doi:10.1088/1748-0221/12/01/P01020`, `arXiv:1609.02366`.

[25] Particle Data Group Collaboration, "Review of particle physics", *PTEP* **2022** (2022) 083C01, `doi:10.1093/ptep/ptac097`.

[26] T. Sjöstrand et al., "An introduction to PYTHIA 8.2", *Comput. Phys. Commun.* **191** (2015) 159, `doi:10.1016/j.cpc.2015.01.024`, `arXiv:1410.3012`.

[27] D. Lange, "The EvtGen particle decay simulation package", *Nucl. Instrum. Meth. A* **462** (2001) 152, `doi:10.1016/S0168-9002(01)00089-4`.

[28] N. Davidson, T. Przedzinski, and Z. Wąs, "PHOTOS interface in C++: technical and physics documentation", *Comput. Phys. Commun.* **199** (2016) 86, `doi:10.1016/j.cpc.2015.09.013`, `arXiv:1011.0937`.

[29] GEANT4 Collaboration, "GEANT4—a simulation toolkit", *Nucl. Instrum. Meth. A* **506** (2003) 250, `doi:10.1016/S0168-9002(03)01368-8`.

[30] N. L. Johnson, "Systems of frequency curves generated by methods of translation", *Biometrika* **36** (1949) 149, `doi:10.1093/biomet/36.1-2.149`.

[31] M. J. Oreglia, "A study of the reactions $\psi' \to \gamma\gamma\psi$". PhD thesis, Stanford University, 1980. SLAC-R-236.

[32] S. Jackman, "Bayesian analysis for the social sciences". John Wiley & Sons, New Jersey, USA, 2009. `doi:10.1002/9780470686621`.

[33] CMS Collaboration, "Tracking POG results for pion efficiency with the D* meson using data from 2016 and 2017", CMS Detector Performance Report CMS-DP-2018-050, 2018.

[34] HEPData record for this analysis, 2022. `doi:10.17182/hepdata.134069`.

A   Numerical results in bins of p_T and $|y|$

Tables A.1 and A.2 provide the numerical $\mathcal{R}_s$ results in bins of p_T and $|y|$, respectively, as shown in Fig. 2. Tables A.3 and A.4 provide the numerical f_d / f_u results in bins of p_T and $|y|$, respectively, as shown in Fig. 3. Besides the central values, the tables include the statistical and systematic uncertainties for each bin. All the results are affected by an extra systematic uncertainty of 2.3%, independent of p_T and $|y|$, associated to the track reconstruction efficiency. The f_d / f_u results are also affected by an extra global systematic uncertainty of 4.3%, reflecting branching fraction uncertainties.

Table A.1: The measured $\mathcal{R}_s$ values as a function of p_T, with the statistical (σ_{stat}) and bin-to-bin systematic (σ_{sys}) uncertainties, in percent. All the results are also affected by an extra global systematic uncertainty of 2.3%, reflecting the track reconstruction efficiency.

p_T (GeV)	$\mathcal{R}_s$	σ_{stat} (%)	σ_{sys} (%)
12–13	0.1314	2.1	3.1
13–14	0.1196	1.6	2.7
14–15	0.1165	1.3	2.4
15–16	0.1154	1.2	2.6
16–18	0.1135	0.8	2.6
18–20	0.1106	0.8	2.8
20–23	0.1105	0.7	2.9
23–26	0.1110	0.8	2.6
26–29	0.1091	0.9	3.2
29–34	0.1095	0.9	2.3
34–45	0.1088	0.9	2.8
45–70	0.1117	1.3	2.6

Table A.2: The measured $\mathcal{R}_s$ values as a function of $|y|$, with the statistical (σ_{stat}) and bin-to-bin systematic (σ_{sys}) uncertainties, in percent. All the results are also affected by an extra global systematic uncertainty of 2.3%, reflecting the track reconstruction efficiency.

$|y|$	$\mathcal{R}_s$	σ_{stat} (%)	σ_{sys} (%)
0.00–0.25	0.1110	0.6	1.8
0.25–0.50	0.1104	0.6	2.0
0.50–0.75	0.1100	0.6	1.9
0.75–1.00	0.1126	0.7	3.9
1.00–1.30	0.1117	0.8	4.3
1.30–1.60	0.1069	1.0	4.3
1.60–2.40	0.1099	1.0	4.4

Table A.3: The measured $f_\mathrm{d}/f_\mathrm{u}$ values as a function of p_T, with the statistical (σ_stat) and bin-to-bin systematic (σ_sys) uncertainties, in percent. All the results are also affected by an extra global systematic uncertainty of 4.9%, reflecting the track reconstruction efficiency and the branching fractions needed to convert $\mathcal{R}_\mathrm{d}$ into $f_\mathrm{d}/f_\mathrm{u}$.

p_T (GeV)	$f_\mathrm{d}/f_\mathrm{u}$	σ_stat (%)	σ_sys (%)
12–13	0.993	3.9	7.8
13–14	1.094	3.4	5.6
14–15	1.006	2.8	4.4
15–16	1.012	1.7	3.3
16–18	1.011	1.1	3.9
18–20	1.036	1.3	3.8
20–23	1.050	1.4	5.1
23–26	1.043	1.4	4.1
26–29	1.056	1.1	4.6
29–34	1.042	1.1	3.8
34–45	0.999	0.8	2.5
45–70	0.983	1.9	2.4

Table A.4: The measured $f_\mathrm{d}/f_\mathrm{u}$ values as a function of $|y|$, with the statistical (σ_stat) and bin-to-bin systematic (σ_sys) uncertainties, in percent. All the results are also affected by an extra global systematic uncertainty of 4.9%, reflecting the track reconstruction efficiency and the branching fractions needed to convert $\mathcal{R}_\mathrm{d}$ into $f_\mathrm{d}/f_\mathrm{u}$.

$|y|$	$f_\mathrm{d}/f_\mathrm{u}$	σ_stat (%)	σ_sys (%)
0.00–0.25	1.020	0.9	2.3
0.25–0.50	1.034	0.9	2.4
0.50–0.75	1.028	0.8	2.3
0.75–1.00	1.038	0.9	4.5
1.00–1.30	1.024	0.9	4.9
1.30–1.60	1.002	1.0	4.2
1.60–2.40	0.992	0.6	4.3